Accepted for publication in *The Astrophysical Journal*, August 15, 2005
Preprint typeset using LaTeX style emulateapj v. 6/22/04

EVOLUTION OF FIELD EARLY-TYPE GALAXIES: THE VIEW FROM GOODS/CDFS

Ignacio Ferreras[1], Thorsten Lisker[2], C. Marcella Carollo and Simon J. Lilly
Institut für Astronomie, ETH Zürich, CH-8093 Zürich, Switzerland

and

Bahram Mobasher
Space Telescope Science Institute, 3700 San Martin Drive, Baltimore, MD 21218, USA
Accepted for publication in The Astrophysical Journal, August 15, 2005

ABSTRACT

We explore the evolution of field early-type galaxies on a sample extracted from the ACS images of the Southern GOODS field. The galaxies are selected by means of a non-parametric analysis followed by visual inspection of the candidates with a concentrated surface brightness distribution. We furthermore exclude from the final sample those galaxies which are not consistent with an evolution into the Kormendy relation between surface brightness and size that is observed for $z = 0$ ellipticals. The final set – which comprises 249 galaxies with a median redshift $z_m = 0.71$ – represents a sample of early-type systems *not* selected with respect to color, with similar scaling relations as those of bona fide elliptical galaxies. The distribution of number counts versus apparent magnitude rejects a constant number density with cosmic time and suggests a substantial decrease with redshift: $n \propto (1+z)^{-2.5}$. The majority of the galaxies (78%) feature passively evolving old stellar populations. One third of those in the upper half of the redshift distribution have blue colors, in contrast to only 10% in the lower redshift subsample. An adaptive binning of the color maps using an optimal Voronoi tessellation is performed to explore the internal color distribution. We find that the red and blue early-type galaxies in our sample have distinct behavior with respect to the *color gradients*, so that most blue galaxies feature blue cores whereas most of the red early-types are passively evolving stellar populations with red cores, i.e. similar systems to local early-type galaxies. Furthermore, the color gradients and scatter do not evolve with redshift and are compatible with the observations at $z = 0$ assuming a radial dependence of the metallicity within each galaxy. Significant gradients in the stellar age are readily ruled out. This work emphasizes the need for a careful sample selection, as we found that most of those galaxies which were visually classified as candidate early types – but then rejected based on the Kormendy relation – feature blue colors characteristic of recent star formation.

Subject headings: galaxies: elliptical and lenticular, cD - galaxies: evolution - galaxies: stellar content

1. INTRODUCTION

The formation of early-type galaxies poses one of the most intriguing riddles of astrophysics. Their stellar populations reveal an early formation process, with no major star formation at redshifts $z \lesssim 2$ (e.g. Bower, Lucey & Ellis 1992; Stanford, Eisenhardt & Dickinson 1998). Recent findings of spheroidal galaxies at $z \gtrsim 1$ with a massive stellar component ($\gtrsim 10^{11}$ $M_\odot$) already in place confirms this early buildup. Furthermore, these red and old galaxies make a 30% contribution to the total stellar mass content in the Universe at $z \sim 1-2$ (Glazebrook et al. 2004; Cimatti et al. 2004). The tight correlation between color and luminosity and its evolution with redshift implies a mass-metallicity relation (Kodama & Arimoto 1997; Kuntschner 2000). Furthermore, the observed enhancement of [Mg/Fe] in giant ellipticals with respect to solar abundance ratios (e.g. Carollo, Buson & Danziger 1993; Carollo & Danziger 1994a,1994b; Trager et al. 2000; Eisenstein et al. 2003) implies a very short period of formation which should not be any longer than 1 Gyr (e.g. Thomas, Greggio & Bender 1999). Hence, the photo-spectroscopic properties of giant early-type galaxies consistently reveals an early, intense and brief period of star formation inside a deep potential well.

On the other hand, our current knowledge of structure formation suggests a hierarchical buildup, so that small galaxies form first and massive galaxies and clusters of galaxies assemble later (e.g. White & Rees 1978). Semi-analytical models have combined simulations of structure formation to simple prescriptions of star formation (e.g. Baugh et al. 1998; Kaufmann & Charlot 1998; Somerville & Primack 1999) and have come up with significant achievements in our understanding of many properties of galaxy formation. However, these models have also been criticized as being too contrived as many parameters are used and adjusted in order to fit the observations *a posteriori*. The current problem of [Mg/Fe] enhancement in massive ellipticals has posed so far one of the most important challenges to these models (Thomas 1999).

Quite often in the literature an alternative scenario is invoked, namely the monolithic collapse model, based on the early attempts of Eggen, Lynden-Bell & Sandage (1962) at explaining the formation of our Milky Way. According to this model the Galaxy formed very early and in a rapid collapse. The extension to early-type galaxies assumes a highly efficient formation process so that most

[1] Current address: Department of Physics and Astronomy, University College London, Gower Street, London WC1E 6BT, United Kingdom
[2] Current address: Astronomical Institute, University of Basel, Venusstrasse 7, CH-4102 Binningen, Switzerland

of the stellar populations are formed early, followed by pure passive evolution. Such a model is compatible with the stellar populations of early-type galaxies as discussed above. However, monolithic collapse does not include any information on the constraints that the cosmology imposes on structure formation.

The main drawback in the study of early-type galaxies at moderate and high redshift lies in the sample selection. The outstanding spatial resolution of the Hubble Space Telescope has enabled these searches in the past few years. The Wide Field and Planetary Camera 2 (WFPC2) and the more recent Advanced Camera for Surveys (ACS) allow a resolved analysis of the projected surface brightness profiles for galaxies with characteristic sizes down to ~ 0.1 arcsec, which maps into a physical projected size of ~ 1 kpc at $z = 1$ for our chosen cosmology (see below). Deep surveys such as the Hubble Deep Fields probe deep enough to allow a resolved color map of early-type galaxies at moderate and high redshift (e.g. Tamura & Ohta 2000; Menanteau, Abraham & Ellis 2001).

Recent surveys targeting early-type galaxies at moderate and high redshift (e.g. Franceschini et al. 1998; Schade et al. 1999; Stanford et al. 2004) have come up with a common picture, namely that these galaxies have most of their stellar populations formed before $z \gtrsim 2$ in agreement with previous studies. No significant differences are found between cluster and field early-type galaxies (van Dokkum et al. 2001). However, there is evidence for a redshift evolution of the size and stellar mass content (Fasano et al. 1998; Trujillo & Aguerri 2004; Bell et al. 2004; Fontana et al. 2004). Furthermore, the resolved color analysis of samples of early-type galaxies in the HDF (Menanteau et al. 2001) and in the field of the Tadpole galaxy (Menanteau et al 2004) have revealed that $\sim 20\%$ of the sample of galaxies classified as early-types present blue cores characteristic of recent or ongoing star formation. Moreover, spectroscopy has also revealed [O II] emission lines in a similar fraction of field early-type galaxies (Schade et al. 1999; Treu et al. 2002).

However, all these analyses critically hinge on the criterion used to determine whether a galaxy belongs to an early-type morphology or not. There are two main approaches to define such a type: either through its morphology or its stellar populations. The latter is a fairly straightforward method to use and indeed has been the main selection criterion of many surveys (e.g. Bell et al. 2004). However, this method only targets a predefined set of stellar populations. Ellipticals with a significant amount of star formation would be misclassified in this way.

A morphological analysis allows us to compare the same type of objects locally and at high redshift. In this paper, we start with a non-parametric approach for the classification (e.g. Abraham et al. 1994). We believe this method is very robust for the faint and small galaxies found in high redshift surveys, especially when complemented by subsequent visual inspection. We pay special attention to the sample selection and throughout this project we question whether the selected objects are indeed early-type galaxies. The sample is also split with respect to the observed optical and NIR colors as classified by Mobasher et al. (2004). Different tests regarding the color distribution, surface brightness and size will lead us to reject most of the bluer systems. This is a result with important consequences in the interpretation of present and upcoming surveys of early-type galaxies.

Throughout this paper we use a concordance ΛCDM cosmology with $\Omega_m = 0.3$ and $H_0 = 70$ km s^{-1} Mpc^{-1}. For this cosmology, the age of the Universe is 13.5 Gyr and the look back times at $z = 0.5$ and $z = 1$ are 5.0 and 7.7 Gyr, respectively. All magnitudes are given in the AB system.

2. THE DATA

Our sample is selected from the v1.0 release of the HST/ACS images of the GOODS-South field (Giavalisco et al. 2004). These images cover a 160 arcmin^2 area towards the Chandra Deep Field South, and consist of four deep images through the F435W(B), F606W(V), F775W(i) and F850LP(z) passbands of ACS. The field is divided into 18 sections and the images are drizzled with a pixel size of 30 mas – chosen to optimize the sampling of the PSF. Each image comes with a weight map given as the expected inverse variance per pixel. The weight maps are used both to assess uncertainties in the direct measurements as well as to generate mock images of early-type galaxies in order to perform a Monte Carlo analysis of the accuracy of the color gradients and scatter (see appendix).

Central to this project is a redshift estimate and a photometric classification. We use the photometric redshift catalog of Mobasher et al. (2004) as well as the spectroscopic follow-up from the VLT/FORS2 (Vanzella et al. 2005) and VLT/VIMOS (Le Fèvre et al. 2004) redshift surveys. The photometric redshifts of Mobasher et al. (2004) have an RMS scatter with respect to the spectroscopic measurements of $\sigma(\Delta z/1+z) \leq 0.1$. The "photometric" type is a byproduct of the classification and corresponds to the template that gives the best fit to the photometric data. This type ranges from 1 (early-type galaxy) to 6 (starburst) and is interpolated in steps of 1/3. Our classification does *not* reject candidates based on this photometric type, i.e. our sample is not biassed in favor of red galaxies. However, in order to explore the connection between the morphological and photometric classification, we decided to separate the final sample (see §3 and §4) with respect to photometric types, so that galaxies with a type $t \leq 1\frac{1}{3}$ are termed red galaxies and $t > 1\frac{1}{3}$ are blue galaxies.

3. MORPHOLOGICAL CLASSIFICATION

In order to create a first object catalog, source detection was performed in the F775W band using the Source Extractor Software (hereafter SExtractor, Bertin & Arnouts 1996). Even though the reddest band would be the obvious choice when exploring a large range of redshifts, we discarded the F850LP bandpass as the images through this filter are not as deep as in the F775W passband. From SExtractor, we obtained segmentation images – which define the pixels associated to each object – for a signal threshold of $1\,\sigma$. We used these as input for the computation of an elliptical aperture for each source, with the ellipticity and position angle derived from the image moments (e.g. Abraham et al. 1994), and the semi-major axis (SMA) chosen to be 1.0 'Petrosian SMA'. The latter means that we applied the concept of the Petrosian

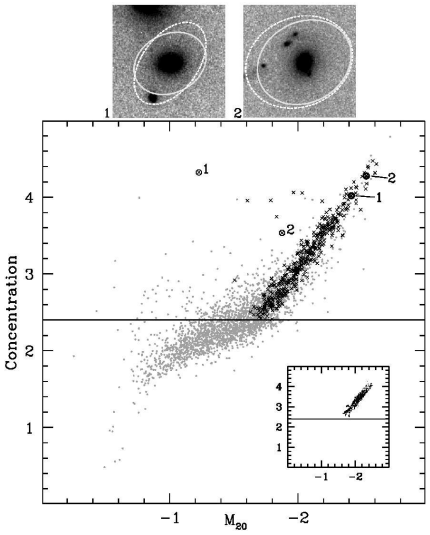

FIG. 1.— The C-M_{20}-distribution of all galaxies with $i_{\rm AB} \leq 24$: visually selected early-types (black crosses) and the rest (grey dots). The F775W images of two galaxies are shown above the diagram, and their positions before and after the manual replacement of neighboring sources are labeled. Both images show the Petrosian aperture before (dashed line) and after the replacement. (Note that this replacement is not applied to the images shown here, i.e. all sources are still there.) The inset shows the C-M_{20}-distribution of simulated galaxies (see text).

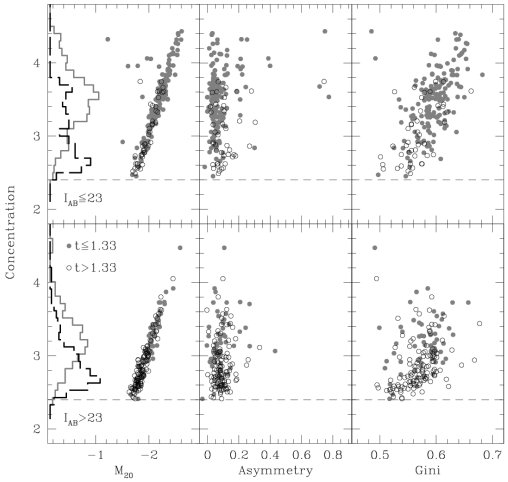

FIG. 2.— The morphological estimates of concentration, asymmetry, M_{20}, and the Gini coefficient are shown for our final sample, split into bright (*top*) and faint (*bottom*) galaxies, divided roughly at the value of the median ($i_{\rm AB} = 22.9$). Throughout the paper we divide the sample into red (filled circles; $t \leq 1\frac{1}{3}$) and blue galaxies (hollow circles; $t > 1\frac{1}{3}$). The dashed line signals the main selection criterion, namely $C > 2.40$. The histograms of the red and blue subsamples are shown in the left panels.

radius (Petrosian 1976). It is chosen so that the ratio between the surface brightness at that radius (r_p) and the average one inside r_p is fixed at a constant value: $\eta \equiv \Sigma(r_p)/\langle\Sigma(\leq r_p)\rangle = 0.2$ (see e.g. Lotz et al. 2004). We used elliptical apertures defined by the image moments of the initial segmentation image. Choosing elliptical instead of circular apertures guarantees that we do not unnecessarily include a large number of noise-dominated pixels, which is important for obtaining reliable morphological parameters.

Although previous studies preferentially used apertures of 1.5 Petrosian SMA (e.g. Lotz et al. 2004), it seemed more useful for the identification of concentrated objects to choose 1.0 Petrosian SMA: first, we avoid for all types of galaxies the inclusion of noise-dominated pixels into the aperture, which overall allows a more robust classification, and second, we lower the amount of contamination by nearby sources. Due to this approach, we miss a certain fraction of the galaxy light (see e.g. Blanton et al. 2001), but since this is consistently applied throughout the paper, it does not prevent us from benefiting from the advantages named above.

Still, in order to obtain a useful Petrosian SMA, it was inevitable to replace all sources – as defined by the segmentation image – in the vicinity of the current object by random gaussian noise matching the background properties, following the approach of Conselice et al. (2005). These neighbors would confuse not only the Petrosian SMA, but also the morphological parameters derived subsequently. Note that the fraction of objects whose aperture would be significantly affected by one or more nearby sources is 13%. In addition, we performed a proper background subtraction as described in §§6.2.

Magnitudes were derived using the final aperture, and all objects with $i_{\rm AB} > 24.0$ were excluded, with 2,837 galaxies remaining. We then computed model-independent morphological parameters on that aperture, namely central concentration (C, Bershady et al. 2000), asymmetry (A, Conselice et al. 2000), the Gini coefficient (G, Lotz et al. 2004), and M_{20} (Lotz et al. 2004). Our goal was to find an appropriate selection criterion using these parameters, which on the one hand should guarantee inclusion of all (potential) spheroids, but on the other hand should exclude the maximum number of non-spheroids.

We show in Figure 1 that basically all galaxies follow a linear relation in the C-M_{20}-plane, which changes its slope at about C=2.5, $M_{20} = -1.7$. From the definition of the two parameters, we deduce that this marks the transition between bulge-dominated and disk-dominated objects: M_{20} traces the spatial distribution of the brightest 20% of all object pixels, *no matter where* they are located, while C is sensitive to the *central* brightest 20%. It follows that, at the point when the disk – or more general: the outer part of a galaxy – starts contributing to the *total* 20%, the M_{20} increases fast, represented by the lower part of the sequence. We therefore decided to exclude all galaxies with a concentration below $C = 2.4$, since they lie below the transition point, allowing for an uncertainty of 0.1. This leaves us with a subsample of 1,540 candidate early type galaxies, or 54% of the full sample.

Four of us (I.F., T.L., C.M.C., S.J.L.) subsequently performed independent visual classification for the whole candidate sample, inspecting all four GOODS/ACS bands. A galaxy was included in the sample if three people classified it as E/S0. We selected 372 galaxies from the list of 1,540 candidates. Furthermore, we revisited the sub-sample of 274 galaxies which were clas-

sified by only 1 or 2 of us as early types. In this second pass, a galaxy was included in the final list if 3 of us independently decided favorably. This increased the list to an additional eight members, for a total of 380 early-type galaxies, or 25% of the candidates (see §6 for a discussion of this small fraction). This sample was cross-correlated with the photometric redshift catalog of Mobasher et al. (2004) and the GOODS ACS catalog v1.1 and constitutes our visually classified sample, shown as black crosses in Figure 1.

Nine of these objects do not fall on the linear relation, but instead show a higher M_{20} value. Two of these are contaminated by bright artifacts that frequently occur on the edges of the GOODS ACS v1.0 images, whereas the other seven have one or more very close or even connected neighbors. These contaminants had not been deblended in the SExtractor segmentation images. However, by manually replacing the contaminants with noise where they are not too close to the main object, we show in Figure 1 that the parameters of all our objects fall onto the observed $C-M_{20}$-relation: the objects labeled 1 and 2 first occupy the left position marked with the corresponding number, but after the manual replacement, they switch to the marked positions on the right.

When we neglect objects that do not follow the $C-M_{20}$ relation, we can apply cuts around our sample in the multidimensional parameter space, in order to see whether a more efficient early-type candidate selection would be possible. By choosing $C \geq 2.40$, $M_{20} \leq -1.60$, $G \geq 0.48$, $A \leq 0.35$, we end up with $1,099$ candidate early types, thus increasing the fraction of visually classified early types to 34%. The visually classified sample is shown in figure 2 as a function of the morphological parameters explored in this paper. Red and blue galaxies are coded as grey and hollow circles, respectively (see below). The panels on the left also show the histogram of the concentrations for red and blue galaxies as a solid and dashed line, respectively.

Several authors have advertised the use of model-independent morphological parameters for galaxy classification (e.g. Lotz et al. 2004, Conselice 2003). Therefore, it might appear surprising that our morphological pre-selection was not able to exclude more than 46% of the initial sample, and that only one quarter of the so selected objects passed the subsequent visual classification. There is, however, a major difference in the application of those parameters between our study and the ones named above: while the latter aimed at a *statistical* segregation of galaxy types, it has been our goal to obtain a *complete* sample of early type galaxies. If we instead wanted to present only a rough dividing line of early and late type objects, a possible choice would be $C > 3$, since this includes 75% of our final sample while excluding 90% of other galaxies. However, given the range of simulated early-type objects shown in Fig. 1 as well as our successful selection of a complete sample (see §4), it is clear that the goal of completeness can only be achieved through a selection process like the one presented in this paper.

4. PHOTOMETRIC CLASSIFICATION

Our preliminary visual classification selects objects with a concentrated surface brightness profile. Bright nuclei or knots of star formation – when viewed at lower signal-to-noise ratios and with apparent sizes close to the resolution limit of the ACS images – can be classified as early-type galaxies. We decided to impose a further constraint on our sample, based on the observed scaling relations of early-type galaxies. The way we choose to ascertain the connection between our sample and local elliptical galaxies is through the Kormendy relation (Kormendy 1977). This is one of the projections of the Fundamental Plane and correlates the size and the rest frame average surface brightness inside the effective radius. The Kormendy relation is a powerful and "cheap" technique since it only involves photometry, and it is found to hold at $z > 0$ (La Barbera et al. 2003). Figure 3 shows the Kormendy relation for our sample, separated into a low- (*bottom*) and high-redshift subsample (*top*). We show the surface brightness in the rest frame B band, which requires a K correction from a nearby observed filter. We have applied the photometric type in order to choose the template SED needed to estimate the K correction. The grey and hollow circles correspond to red and blue galaxies, respectively. The stars are Coma cluster galaxies (Jørgensen, Franx & Kjærgaard 1995) and the lines represent the best fit and scatter.

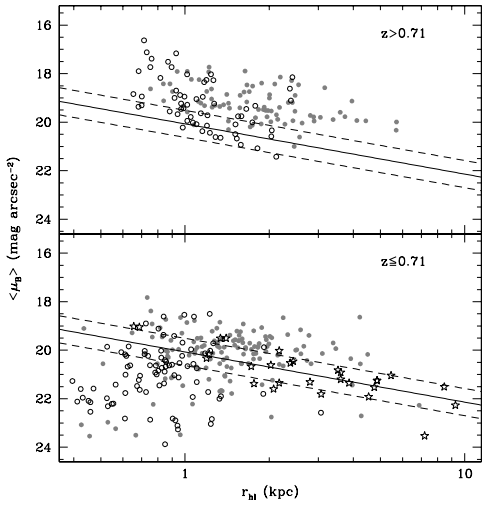

FIG. 3.— Rest frame B-band Kormendy relation. Our sample is subdivided into red (grey dots; $\leq 1\frac{1}{3}$) and blue galaxies (hollow circles). The K correction is performed using the spectral templates used in the determination of the photometric types. The K correction is chosen as the smallest one between the observed V band or I band and the rest frame B band. The stars give the Coma cluster relation from Jørgensen, Franx & Kjærgaard (1995), whose best linear fit is given by the solid line and dashed lines (biweight scatter).

The figure shows a remarkable segregation with respect to color. Notice the large number of blue galaxies in the bottom panel which fall below the dashed lines that mark the local relation. Passive fading of the stellar populations implies that these galaxies will evolve with redshift towards fainter surface brightness, drifting away from the relation found in present day early-type galaxies. This suggests that most of the blue galaxies at $z \leq 0.71$ are not early-type galaxies, whereas most of the red galaxies plus some of the high-redshift blue galaxies at $z > 0.71$ would qualify as bona fide early-type systems.

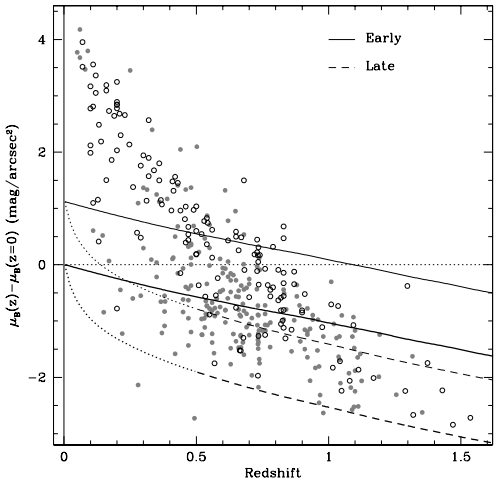

FIG. 4.— Difference between the average surface brightness (at the observed redshift of each galaxy in the rest frame B band) and the local measurement expected from the Kormendy relation, as a function of redshift. The evolution of two star formation histories with a formation redshift $z_F = 5$ is shown. The thick solid line corresponds to an exponentially decaying star formation rate with timescale $\tau_{SF} = 0.5$ Gyr (labelled Early). The thick dashed line assumes a constant star formation rate from $z_F = 5$ to the observed redshift followed by a truncation of the SFR (labelled Late). The thin lines are equivalent to the previous star formation histories with an offset of 2× scatter found in local galaxies. Notice the dashed line becomes dotted at $z < 0.5$. At these redshifts, such models would be in conflict with the photometry of local early-type galaxies.

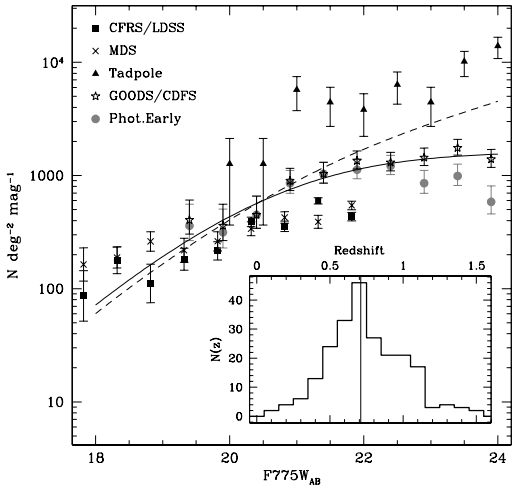

FIG. 5.— Number counts of early-type galaxies in the GOODS/CDFS field (stars) compared to the CFRS/LDSS redshift surveys (Brinchmann et al. 1998), the Medium Deep Survey (MDS; Abraham et al. 1996) and the high-redshift field sample towards the Tadpole field (Menanteau et al. 2004). Our sample is also shown for the subsample of red early-types ($t \leq 1\frac{1}{3}$; filled circles). Poisson error bars are shown. The lines give two number density predictions using the local luminosity function of E/S0s of Marzke et al. (1998). The dashed line assumes a constant comoving density and includes the photometric evolution of a typical early-type galaxy (see text for details). The solid line adds to the color evolution a change in the comoving number density $n \propto (1+z)^{-2.5}$. The inset gives the redshift distribution of our sample, with the median at $z_m = 0.71$.

We can thereby select only those galaxies which will evolve into the observed local Kormendy relation. Figure 4 shows the change between the observed surface brightness and the one corresponding to the Kormendy relation for a given r_{hl} as a function of redshift. The sample is divided into red (grey dots) and blue galaxies (hollow dots) as usual. The thick solid line gives the evolution of an exponentially decaying star formation rate which started at $z_F = 5$ with a timescale $\tau_{SF} = 0.5$ Gyr, and the dashed line corresponds to a constant SFR truncated at the observed redshift, both with solar metallicity (population synthesis models from Bruzual & Charlot 2003). Both formation histories are required to have $\Delta\mu_B = 0$ at $z = 0$. Notice the dashed line becomes dotted at $z < 0.5$ to represent the fact that an extended star formation history at those redshifts would be in conflict with the photometry of early-type galaxies. The thin lines are offsets of the previous formation histories by 2× the observed scatter found in the local sample (Jørgensen et al. 1995). The threshold imposed depends on the photometric type, as defined in Mobasher et al. (2004). We interpolate between these two extreme SFHs, so that the thin solid line is the limit for a type=1 (red) galaxy and the thin dashed limit corresponds to a starburst (type=6). All galaxies which fall above their corresponding threshold will evolve with age into a region outside of the Kormendy relation. The Kormendy-consistent sample comprises 249 galaxies, i.e. about 70% of the visually selected sample, with a significant rejection of blue galaxies. In fact, 90% of the blue $z \leq 0.71$ subsample are rejected, whereas only 34% are rejected in the higher redshift case. In contrast, most of the red systems are included in the final list: only 12% of these galaxies are rejected.

The rejection process eliminates 50% of faint galaxies ($i_{\rm AB} > 23$) and only 18% of the brighter subsample ($i_{\rm AB} \leq 23$). Even though the i-band ACS images of the GOODS field reach a 10σ limiting magnitude of $i_{\rm AB} = 27.1$ with a 30 mas sampling and ~ 100 mas resolution, about one third of the visually classified objects must be rejected. A $i_{\rm AB} = 24$ limit can be taken as a reasonable magnitude limit for the visual classification in these images. Within that limit it is unlikely that we have missed any early-type galaxy. First, simulated galaxy images with a Sérsic surface brightness profile with indices between $3-4$ and similar magnitudes and sizes of those in the real sample cover the range $2.5 < C < 4.3$, and thus lie clearly above our cut of $C = 2.4$ (Figure 1). Second, the majority of galaxies that are close to the lower concentration end are faint ($i_{\rm AB} \geq 23$), small ($r_{\rm hl} \leq 0.2$ arcsec), blue objects, suggesting regions of star formation instead of *bona fide* early-type galaxies. Third, we went back to the photometric redshift catalog and searched for red galaxies below the concentration threshold imposed – since they constitute the majority of our final sample. We found a total of 30 objects (with $C < 2.4$) whose images clearly do not correspond to an early type morphology.

5. NUMBER COUNTS

Figure 5 shows the number counts as a function of apparent magnitude ($i_{\rm AB}$) from our sample (stars), com-

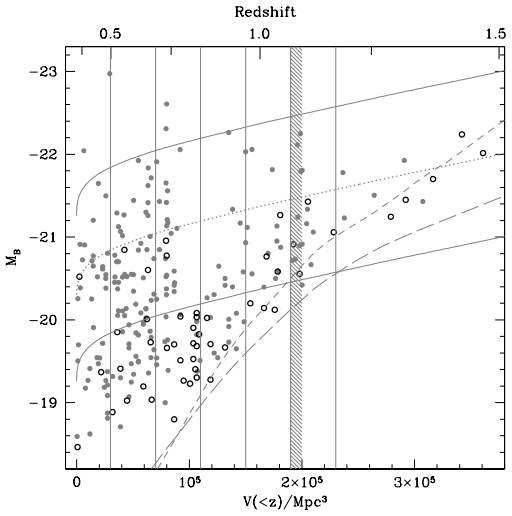

FIG. 6.— Distribution in absolute luminosity as a function of enclosed comoving volume. This figure allows us to determine the luminosity function of the sample since the number of galaxies inside equal segments along the horizontal axis (as shown by the vertical lines) corresponds to the number of galaxies inside the same comoving volume. The thick dotted line tracks the evolution of a $M_\star$ galaxy using a star formation history with solar metallicity, formation redshift $z_F = 5$ and star formation timescale $\tau_{SF} = 0.5$ Gyr. The thick solid lines represent $M_\star \pm 1$ mag used to determine a simple luminosity function as shown in the next figure. The thin lines mark the $i_{\rm AB} \leq 24$ limiting magnitude for a red (short dashed) and blue galaxy (long dashed). The shaded region indicates that the last redshift bin starts showing a significant incompleteness for red spheroids.

pared to the number counts from the CFRS/LDSS survey (squares; Brinchmann et al. 1998) and the Medium Deep Survey (crosses; Abraham et al. 1996). The sample of field early-type galaxies in the HST/ACS image of the Tadpole galaxy is also shown (triangles; Menanteau et al. 2004). Our subsample of red galaxies is shown as filled dots. The Tadpole sample yields a remarkably large number density of objects, with a large fraction of blue cores[3]. We believe this large density is caused by their broader visual definition of an early-type galaxy. Indeed, a significant fraction of their candidates would have been selected by us as late-type systems. The dashed line represents a pure luminosity evolution model (i.e. fixed comoving density) and uses the K correction corresponding to an exponentially decaying star formation rate starting at $z_F = 5$ with $\tau_{SF} = 0.5$ Gyr and solar metallicity. In order to determine the number counts we use the local luminosity function of early-type galaxies from Marzke et al. (1998) adapted to our cosmology. The solid line gives the number counts assuming a decrease of the comoving number density of galaxies as $n \propto (1+z)^{-2.5}$. Notice the drop of the subsample of red galaxies at $i_{\rm AB} \geq 23$. Given that the ACS images have a limiting magnitude that goes 4 magnitudes fainter than this level, we do not anticipate incompleteness regarding the apparent magnitudes. However, one could expect incompleteness because of spatial resolution. Our selection criterion is robust for galaxies with a $r_{hl} \geq 2$ pixels, which translates into a projected distance of 0.4 kpc at $z = 0.5$ or 0.5 kpc at $z = 1$. Therefore, we should not expect to miss early-type galaxies because of the spatial resolution of the ACS images.

The inset in figure 5 gives the redshift distribution of our final sample (the vertical line gives the median, $z_m = 0.71$), and features a peak in the number of galaxies around $z \sim 0.7$, which is partly caused by the effect of cosmic variance given the field of view (160 arcmin^2; Somerville et al 2004). This is a well-known spike (Gilli et al. 2003) also seen in K20, a K-selected survey of galaxies with a pointing towards the same field (Cimatti et al. 2002). The spatial distribution of the galaxies at $z \sim 0.7$ implies a loose structure rather than a cluster. Despite cosmic variance, most studies, including our own, provide consistent number counts. We therefore use our data to estimate the evolution of the number density of early-type galaxies up to $z \sim 1.2$.

Figure 6 shows the B-band absolute luminosity with respect to the comoving volume out to the observed redshift of each galaxy. It can be interpreted as a luminosity function. The number of galaxies inside equal segments along the horizontal axis gives a comoving number density. The vertical lines show an example of redshift ranges delimiting shells with constant comoving volume ($\Delta V = 4 \times 10^4$ Mpc^3), as used in the next figure. The thick dotted line corresponds to a typical $M_\star$ galaxy and the thick solid lines are offsets ± 1 mag with respect to this value. The limiting magnitude – which depends on the choice of star formation history – is shown as thin short and long dashed lines for a short ($\tau_{SF} = 0.5$ Gyr) or more extended (8 Gyr) SFH, respectively. Counting the galaxies within the cells determined by the vertical lines and the thick lines which track $M_\star$ and $M_\star \pm 1^m$ we can assess the evolution of the number density of galaxies. Notice that the last redshift bin presents a significant imnompleteness in the detection of red spheroids. We have included a shaded region to illustrate this point.

Figure 7 shows these counts including simple Poisson error bars (bottom panel) or a more realistic estimate of the uncertainty by adding in quadrature the cosmic variance (CV) from the models of Somerville et al. (2004) for a correlation function $\xi(r) = (r_0/r)^\gamma$, with $r_0 = 5h^{-1}$ Mpc and $\gamma = 1.8$. The stars and crosses represent the bright and faint luminosity bins, respectively. The shaded region shows the limit at which we have completeness. The arrow and error bar gives the local comoving number density of early-type galaxies from Marzke et al. (1998). Our data show a decrease of a factor ~ 3 in the comoving number density of galaxies *with an early-type morphology* in the redshift interval $z \sim 0.6 - 1.2$. A survey such as COSMOS[4], with its 2 deg^2 field of view will be able to assess the scatter around this factor due to cosmic variance and large scale structure environment.

6. RESOLVED COLOR ANALYSIS

The high resolution, good sampling and depth of the HST/ACS GOODS images enable us to perform a resolved analysis of the color distribution in our sample of early-types. The 30 mas drizzled pixel translates into a

[3] A transformation had to be applied to translate their F814W(Vega) into our F775W(AB) photometry. It amounts to $\sim 0.7 \pm 0.15$ mag, which is still clearly insufficent to reconcile the number counts

[4] See `http://www.astro.caltech.edu/~cosmos`

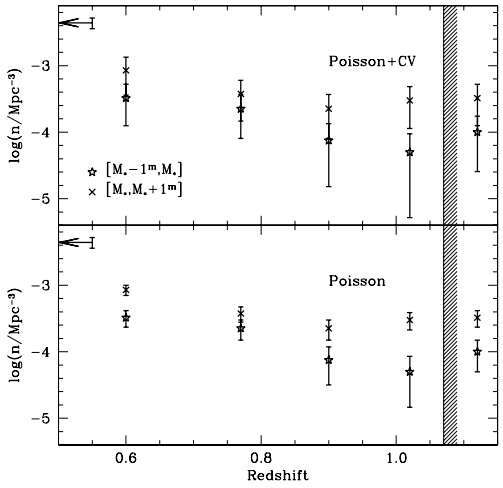

FIG. 7.— The evolution of the luminosity function is shown, according to the data presented in the previous figure. For each redshift bin we give the comoving number density for two luminosity bins around $M_\star$. The bottom panel shows the data along with Poisson error bars. The top panel includes in quadrature the effect of cosmic variance according to the models of Somerville et al. (2004). The shaded area shows the redshift at which the sample is not complete. The arrow and error bar gives the local number density of E/S0 from Marzke et al. (1998).

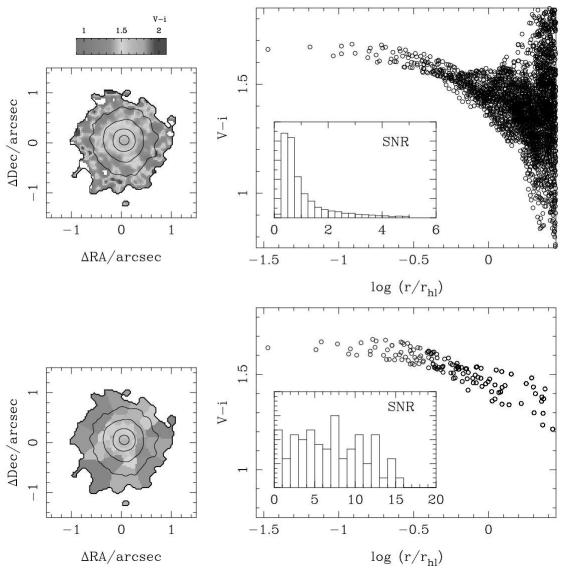

FIG. 8.— Pixel-by-Pixel and Voronoi tessellation analysis of a sample early-type galaxy: GDS J033246.05 − 275444.8 ($i_{\rm AB}$ = 22.14, z = 0.64). The top panels show the results for a pixel by pixel analysis. The image gives the $V-i$ color map and the contours track the surface brightness in the i-band from 21 to 24 in steps of 1 mag/arcsec^2. The bottom panels show the analysis on an adaptive binning following an Voronoi Tessellation as described in the text. The target SNR in the flux ratio $\Phi(V)/\Phi(i)$ is 10, corresponding to a photometric error in $V-i$ of ~ 0.1 mag. The right panels show the color profile and the histogram of SNR in either case.

projected distance of 180 pc at $z = 0.5$ and 240 pc at $z = 1.0$.

A good alignment of the two images is crucial, as offsets down to a fraction of a pixel can generate a fake color gradient – see Zheng et al. (2004) for a comprehensive analysis of this issue. Our images come from the release v1.0 of the GOODS/ACS images, which were specifically corrected for geometric distortion. The alignment of the images have a clipped RMS residual between 1/4 and 1/3 of a pixel. Nevertheless, we decided to check the alignment by comparing the centroids of the F606W and F775W images from our detections. Out of the list of 380 galaxies from the visually classified sample, we found a mean offset below 0.02 pixels, with a RMS below 0.15 pixel. If we use a Sérsic profile and take the worst case scenario, i.e. a 0.15 pixel offset with $r_{\rm hl} = 0.2$ arcsec, we get a maximum color offset below 0.05 mag. The mean gives offsets below 0.01 mag. Hence, we can safely discard misalignments as a possible source of systematic uncertainty in the color gradients. Another source of error may come from the estimates of the background. The v1.0 present a non-negligible background which was carefully estimated and subtracted in our analysis (see §§6.2). Furthermore, we checked the possible effect of a bad background estimate on the color gradients by rerunning our analysis on the sample with either no background correction or twice of the original estimate in each band. No significant change in the color gradients was found.

6.1. *Adaptive Binning*

A pixel-by-pixel analysis is an obvious avenue to pursue in the study of unresolved stellar populations (Menanteau, Abraham & Ellis 2001). However, the steepness of the surface brightness profile of early-type galaxies implies the pixel distribution spans a wide range of signal-to-noise ratios (SNR). Adaptive binning is thereby preferred. One common binning procedure reduces the color information to a one dimensional surface brightness profile done by adding the light inside elliptical annuli. At the cost of smoothing out the color distribution, this method gets the maximum SNR from the data.

Adaptive binning is a better option as it preserves as much of the spatial information as possible. Using a tree structure is the first choice, which starts with the full image of the galaxy as the root and then subdivides it into smaller squares aligned with the axes with the criterion of further subdivisions based on the SNR measured in each square. However, this method is only effective if the observed 2D distribution is smooth enough. Furthermore, the scatter of the SNR about the target value is far from optimal in most cases. Cappellari & Copin (2003) presented an optimal binning algorithm based on a Voronoi tessellation. A local density is defined as the square of the SNR, which reduces the binning algorithm to finding a tessellation that encloses equal masses according to this density. The algorithm includes a morphological criterion in order to generate bins as round as possible, an important feature in our analysis as filamentary bins would greatly distort the color gradients. We decided to base our color analysis on a Voronoi tessellation with a target SNR of 10 for the B/i, V/i or i/z flux ratios. This implies a homogeneous photometric uncertainty of ~ 0.1 mag in the colors.

Figure 8 illustrates the advantage of an adaptive binning technique with respect to a pixel-by-pixel analysis. We compare these two methods with a $i_{\rm AB} \sim 22$ galaxy at $z \sim 0.6$ (GDS J033246.05 − 275444.8). The top panels

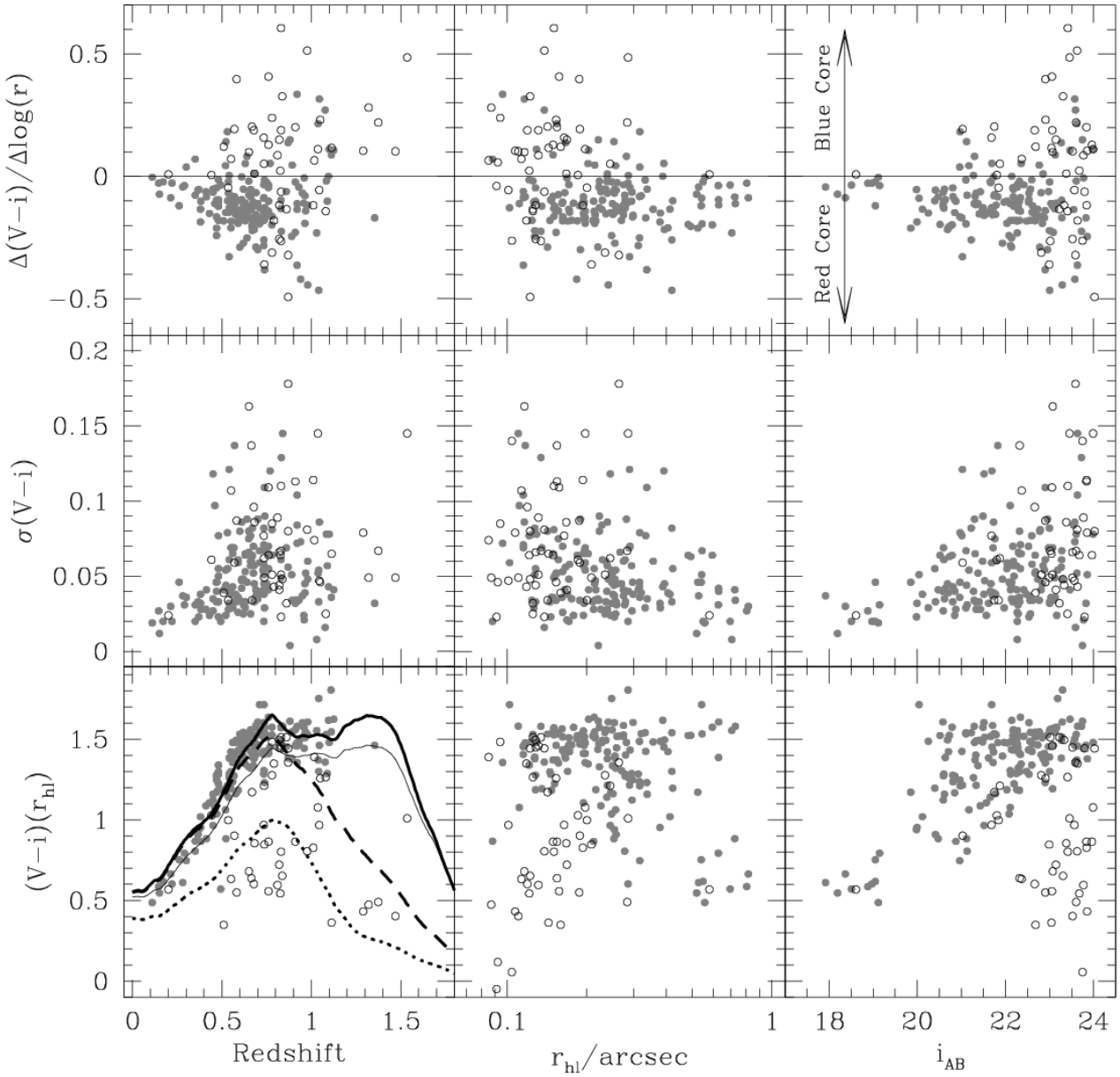

FIG. 9.— $V-i$ color distribution. From top to bottom, the radial color slope, scatter and color at the half-ligh radius of our sample of early-type galaxies is shown as a function of redshift (*left*); half-light radius (*middle*); and i-band apparent magnitude (*right*). The sample is split into those with a photometric type earlier (filled dots) or later (hollow dots) than $1\frac{1}{3}$, which marks the boundary between our selection of red and blue systems. The thick lines in the bottom-left panel give the color evolution of a stellar population with solar metallicity and an exponentially decaying star formation rate, started at $z_F = 5$ and with a decay timescale of 0.5 (solid), 1 (dashed) and 8 Gyr (dotted). The thin solid line shows the evolution with a timescale of 0.5 Gyr at 1/3 of solar metallicity.

show the $V-i$ color map (left) and color-radius distribution (right) along with the distribution of the SNR (inset). The histogram shows a wide distribution with a large number of pixels with SNR$\lesssim 1$. Such a distribution gives a wide scatter of colors in the outer parts of the galaxy. The bottom panels show the same galaxy after an optimal Voronoi tessellation with a target SNR= 10. The color map appears much smoother but not loosing real inhomogeneous color distributions. The histogram of SNR shows that there is a very significant reduction in the number of (binned) pixels with a low SNR. The analysis of the color-radius distribution is thereby more robust and less prone to systematic effects from the noise.

6.2. *Color gradients and scatter*

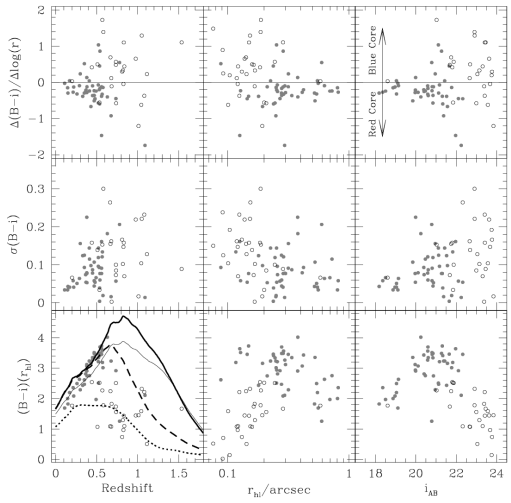

FIG. 10.— Same as figure 9 for $B-i$ color.

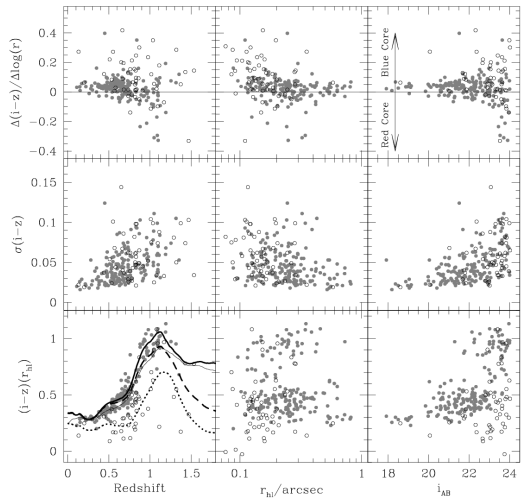

FIG. 11.— Same as figure 9 for $i-z$ color.

For each target, we define the 2D region corresponding to the galaxy from the SExtractor segmentation maps, defined at the 1σ flux level in the deeper i band. The background is estimated in each bandpass by taking the median of the pixels not belonging to the enlarged segmentation map of any source inside a 701×701 pixel region (21×21 arcsec^2) centered at the target. After background subtraction, the resulting image was convolved with the point spread function (PSF) of the other passband used in the analysis. Degrading both images to a common resolution is more robust than deconvolving the images by their PSFs. Deconvolution introduces noise and its effect on the final color maps is hard to assess. We explored two different sets of PSFs, stellar ones from bright stars free of nearby sources and synthetic ones using Tiny Tim (Krist 1993), see appendix for details.

Furthermore, in order to minimize a possible systematic effect from the PSF, we decided to reject pixels inside $r = 0.1$ arcsec from the galaxy centre. These are the pixels most affected by the smearing effect of the PSF, and the simulations show that such a truncation yields results which are insensitive to the choice of PSF. The results presented in this paper are based on a convolution with the – more realistic – stellar PSFs, although a comparison with the second analysis based on the synthetic PSFs indeed show that the color zero points, gradients and scatter do not change significantly.

After the convolution, the image is binned according to a Voronoi tessellation as described above. A linear fit is then applied to the resulting bins as a function of $\log(r/r_{\rm hl})$, where the half-light radius is measured from the Petrosian radius. The fitting method has to be robust not to give much weight to the outliers. Hence, we start fitting the color distribution with an M-estimator based on the mean absolute deviate (Press et al. 1992). We cull the outliers which fall outside of a band extending 4 times the measured scatter with respect to this fit, after which we apply a least-squares fit to a reduced set without these outliers. This result gives the slope and zero point used in our analysis. Finally, the scatter is computed about this linear fit for the full data set. For each galaxy, we thereby come up with three numbers to describe the color distribution, namely zero point (color at $r = r_{hl}$), radial color slope (Δ Color$/\Delta \log r$) and scatter (about the best linear fit to the color radial distribution). The scatter is obtained from the biweight measure of scale (Beers, Flynn & Gebhardt 1990) which is much more robust with respect to the presence of outliers. Nevertheless, we also computed the RMS scatter and found no significant discrepancies between these two estimates of the scatter.

The results for the observed color distribution are shown in figures 9, 10 and 11 for $V-i$, $B-i$, and $i-z$, respectively. The top, middle and bottom panels of the three figures show the color gradient, scatter and color at $r = r_{hl}$ as a function of redshift (*left*), angular size (*middle*) or $i_{\rm AB}$ magnitude (*right*). The sample is subdivided into red (filled dots) and blue (hollow dots) galaxies, as described above. The bottom panels of figures 9, 10 and 11 include the color-redshift evolution of a simple stellar population (Bruzual & Charlot 2003 models; Salpeter IMF) with solar metallicity and formation redshift of $z_F = 5$, with an exponentially decaying star formation rate $\psi(t) \propto \exp(-t/\tau_{SF})$ with timescales $\tau_{SF} = 0.5$ (solid), 1 (dashed) and 8 Gyr (dotted). The thin line corresponds to $\tau_{SF} = 0.5$ Gyr and metallicity $Z_\odot/3$. Notice the remarkable segregation with respect to photometric type. The color segregation should not come as a surprise since the colors themselves are the basis for the photometric classification. However, this segregation is followed by the color gradients, so that objects with blue cores – positive radial color gradients – belong to the late photometric type. Similarly, most of the red objects are found with red cores. Such a behavior is *suggestive* of an inside-out buildup of the stellar component, i.e. all recent star formation (in blue galaxies) takes place at the core, whereas the red galaxies have their oldest populations close to the center. In principle, one could have expected an increased scatter in bluer galaxies – caused by recent star formation. However, the figures do not

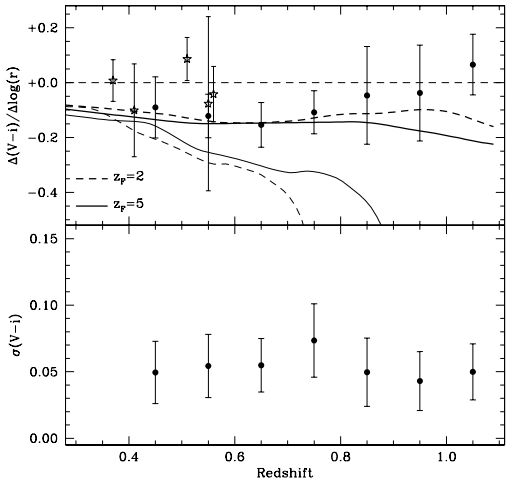

FIG. 12.— $V-i$ gradients (*top*) and scatter (*bottom*) as a function of redshift (only red early-types considered in this figure). The stars are cluster data from Tamura & Ohta (2000). Two alternative evolution models are considered depending on whether the color gradient is caused by metallicity (thick lines) or by age (thin lines). Two formation redshifts are shown for each case: $z_F = 2$ (dashed lines) and $z_F = 5$ (solid lines).

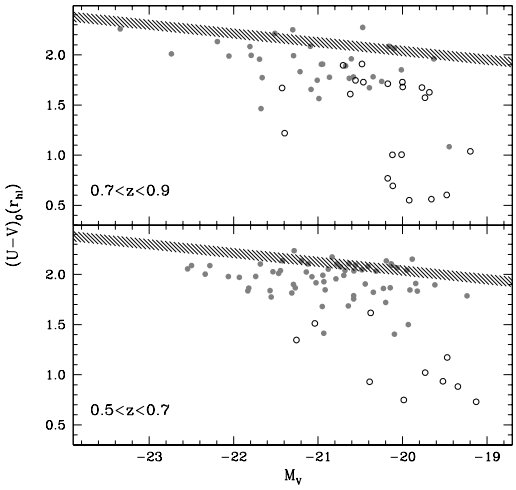

FIG. 13.— The color-magnitude relation in rest frame $U-V$. The shaded area represents the local color-magnitude relation of the Virgo or Coma clusters from Bower et al. (1992). Higher- (top) and lower-redshift subsamples are shown, split at the median redshift, with a redshift interval ($\Delta z = 0.2$) chosen not too large to avoid the scatter from the uncertainties in the K-correction. Filled and hollow circles correspond to our photometric selection of red and blue galaxies, respectively (see text for details).

show such segregation with respect to color, and only display the expected increase in the scatter towards fainter galaxies. This segregation is seen in all three HST/ACS colors (see the top panels of figures 9, 10 and 11).

In figure 12 we present the data in redshift bins, showing the evolution of the color gradient (*top*) and scatter (*bottom*). The stars are cluster data from Tamura & Ohta (2000). We have also included two simple models similar to those presented in Tamura et al. (2000). These two alternative scenarios invoke either a pure age (thin lines) or a pure metallicity radial gradient (thick lines). We used the population synthesis models of Bruzual & Charlot (2003) with a Salpeter IMF. The models are constrained at $z = 0$ by the mean value of $\Delta(B-R)/\Delta \log r = -0.09$ mag/dex from Peletier et al. (1990). For each model we choose two possible ages for the stellar populations at the center: $z_F = 2$ (dashed) and $z_F = 5$ (solid lines).

The data are compatible with a pure metallicity radial gradient and rules out a significant spread in stellar ages within the galaxy. Furthermore, no significant difference is found between our field sample and the cluster galaxies from Tamura & Ohta (2000). The rise in the color gradient at $z \sim 1$ is caused by the larger number of galaxies with blue cores. The lower panel shows the redshift evolution of the scatter, which can be used as a proxy for patchy star formation. No significant change is found with redshift, in support of a quiescent evolution of the stellar populations. The trend found in figure 12 imposes powerful constraints on the formation process of elliptical galaxies, suggesting an early and short-lived formation epoch followed by passive evolution. The galaxies which are undergoing some residual star formation at those epochs are mostly faint and small, supporting a downsizing picture of galaxy formation. The lack of features in the color gradients and the small scatter furthermore suggest that $z < 2$ mergers which lead to early-type galaxies must be essentially dissipationless events.

7. DISCUSSION

An important aspect of our work is that, by construction, we investigate the intermediate redshift population of early-type galaxies which, at those epochs, already look like today's elliptical galaxies. This approach has been followed in other studies of the massive galaxy population at moderate redshift, e.g. to study the color-magnitude relation (Stanford, Eisenhardt & Dickinson 1998) and the fundamental plane (Wuyts et al. 2004; van der Wel et al. 2004). Van Dokkum & Franx (2001) have discussed this issue, christening it the "progenitor bias" as any star-forming galaxy at those epochs – which may nonetheless become part of an elliptical at $z = 0$ – would have been excluded from such analyses. In this respect, we note that the search for intermediate-z red galaxies *without* an early-type morphology that we have conducted on the GOODS/CDFS dataset returns only 30 objects at $i_{\rm AB} \leq 24$. Spitzer and ALMA will help assessing the fraction of dust-enshrouded galaxies which are compatible with their evolution into $z = 0$ early-type galaxies. While ellipticals which are built by a relatively late merger are not accounted in our own and the other quoted investigations, studying the properties of an intermediate-z morphologically-selected sample of ellipticals allows us to explore important issues pertaining to the evolution of massive galaxies. Specifically, the morphological approach allows us not only to set a lower limit on the fraction of the $z = 0$ early-type population which is already in place at $z \sim 1$, but also to investigate whether star formation proceeds in these systems well after their mass assembly has occurred. This is an important constraint to current galaxy formation models.

Figure 13 shows the rest frame $U-V$ color magnitude

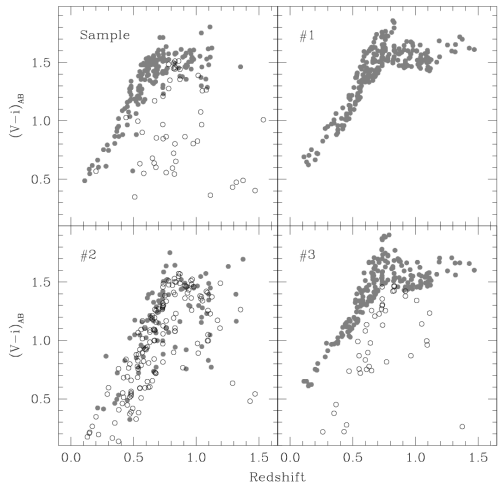

FIG. 14.— Comparison of the observed $V-i$ color vs redshift diagram with a simple model with 2 bursts of star formation. The panel on the top left shows the sample (filled and hollow circles represent red and blue galaxies, respectively). Model #1 assumes a single burst at $z_F = 5$ with a star formation timescale $\tau_{SF} = 0.5$ Gyr, model #2 includes a later second burst in the last 1 Gyr *for all galaxies*. Model #3 imposes this second burst only on 20% of the galaxies (see text for details). The synthetic subsamples are coded depending on whether they have a significant fraction of young stars (hollow circles; $f_Y \geq 0.2$) or are dominated by old stars (filled circles).

relation for two subsamples separated in redshift with respect to the median. A small redshift interval $\Delta z = 0.2$ has been chosen in order to reduce the scatter from the uncertainties in the K correction. The shaded area is the local CMR of the Coma or Virgo cluster (Bower et al. 1992) in the AB system. Notice that practically all red galaxies follow the red sequence except for a systematic blueing caused by the lookback time, as seen in the early-types of clusters at moderate and high redshift (Stanford et al. 1998; Blakeslee et al. 2003). Most of the blue galaxies fall outside of this red sequence, and preferentially represent lower mass systems at higher redshift.

We compare our sample with a simple model which assumes a two-burst formation scenario. Each burst is characterized by an exponentially decaying star formation rate and is formed at times $t(z_F)$ (old) and t_Y (young), respectively:

$$\psi(t) \propto f_Y e^{-(t-t_Y)/\tau_{SF}} + (1-f_Y) e^{-[t-t(z_F)]/\tau_{SF}}, \quad (1)$$

where the star formation timescale is $\tau_{SF} = 0.5$ Gyr, f_Y is the stellar mass fraction in young stars. The old component is formed at $z_F = 5$, and $(t - t_Y) \leq 1$ Gyr, i.e. the young component is formed in the last 1 Gyr. The metallicity is the same for both components but we choose a random value uniformly in the range $-0.3 \leq \log(Z/Z_\odot) \leq +0.3$.

Figure 14 compares the $V-i$ color versus redshift relation with three such models. The top left panel shows our sample. The simulated galaxies have the same redshift distribution as the original sample and are subdivided with respect to their young stellar mass fractions so that the late-types (hollow dots) have $f_Y \geq 0.2$. Model #1 corresponds to a single burst ($f_Y = 0$) for all galaxies. Model #2 assumes a second burst for all galaxies, randomly chosen in the range ($f_Y \leq 0.5$). Finally, model #3 applies this second burst *only* to 20% of the galaxies chosen in a random way. This fraction corresponds to the contribution of blue galaxies to our sample.

As expected, the red galaxies are compatible with a single, early burst scenario – which represents most of the galaxies with a red core. The clear cut separation between the two photometric types can not be explained by a homogeneous distribution of galaxies with a second burst. Model #2 gives a smooth transition between the older and the younger galaxies. However, model #3 shows that the data could be reproduced by a model in which a certain fraction of the galaxies is undergoing a second star forming episode. Some of these galaxies could present the spectral features of a post-starburst E+A galaxy. The fast color evolution along with the finite sampling reproduces the observed bimodality with respect to color. The presence of blue cores in blue galaxies suggest these recent episodes of star formation take place at the centre. Furthermore, figure 13 implies that most of the recent star formation appears in the fainter galaxies, i.e. "down-sizing" (see e.g. Kodama et al. 2004; de Lucia et al. 2004; McIntosh et al. 2005). Such a trend would be expected from a strong correlation between galaxy mass and star formation efficiency as proposed by Ferreras & Silk (2003; 2000a) and is in agreement with various observed properties such as the large scatter at the faint end of the near-ultraviolet – optical color-magnitude relation (Ferreras & Silk 2000b) or the Fundamental Plane of field early-type galaxies at moderate redshift (van der Wel et al. 2004). The "red sequence" of model #3 is compatible with the data out to the highest redshifts and implies that $\sim 95\%$ of the stellar mass component in these galaxies should have been formed ~ 1.5 Gyr after $z_F = 5$, i.e. at redshifts $z \gtrsim 2.5$.

8. SUMMARY AND CONCLUSIONS

The internal color distribution of a large sample of early-type galaxies can be used to constrain the mechanisms leading to the formation and assembly of their stellar populations. In this paper we explore a large sample of field early-types with $i_{\rm AB} \leq 24$ from the HST/ACS images of the GOODS/CDFS field, which cover a solid angle ~ 160 arcmin^2. The classification of early-types starts with a pre-selection of the targets using recent quantitative morphology techniques followed by a visual inspection. A total of 380 objects were selected as early-type galaxies, i.e. with the visual appearance of an elliptical or a lenticular galaxy.

The Kormendy relation is then used to assess which of the candidates will evolve into present day ellipticals. The results shown in figure 3 clearly suggest a dual nature for the blue galaxies. Those at the lower redshifts fall below the local relation, so that – notwithstanding any major structural change – they will evolve away from the Kormendy relation defined by local early-type galaxies. These galaxies are spirals with strong ongoing star formation, or even starbursts. On the other hand, the high-redshift sample of blue galaxies falls within the Kormendy relation. We define a final sample of *bona fide* ellipticals using this criterion. The sample comprises about one third of the original sample where most of the galaxies with blue colors are at the higher redshifts.

TABLE 1
The sample of GOODS/CDFS early-type galaxies.

ID	$i_{\rm AB}$	$r_{\rm hl}$/arcsec	$t_{\rm phot}$	z^a	$\langle V-i\rangle_{\rm rhl}$	$\Delta(V-i)/\Delta\log r$	Scatter
$i_{\rm AB}<23.0$							
J033157.84-274245.2	20.63	0.63	1.00	(0.610)	1.386 ± 0.031	-0.095 ± 0.052	0.04
J033158.13-274459.4	21.02	0.29	1.00	(0.540)	1.215 ± 0.009	-0.328 ± 0.033	0.12
J033159.76-274411.4	21.51	0.25	1.30	(0.450)	0.965 ± 0.031	-0.736 ± 0.114	0.12
J033202.51-274536.0	22.66	0.12	3.00	0.678	0.602 ± 0.007	0.188 ± 0.063	0.10
J033202.71-274310.8	18.51	0.70	1.30	0.493	0.571 ± 0.001	-0.035 ± 0.001	0.02
J033206.88-274207.6	20.96	0.32	1.30	(0.300)	0.747 ± 0.004	0.038 ± 0.012	0.04
J033208.10-274732.7	22.81	0.23	1.70	(0.780)	1.276 ± 0.057	-0.311 ± 0.233	0.05
J033208.41-274231.3	22.03	0.13	1.00	(0.480)	1.186 ± 0.005	-0.101 ± 0.044	0.05
J033208.45-274145.9	22.18	0.24	1.00	(0.660)	1.558 ± 0.030	-0.053 ± 0.119	0.06
J033208.53-274217.7	21.71	0.28	1.00	(0.690)	1.584 ± 0.015	-0.157 ± 0.058	0.04

Note. — A full version of table 1 is published in its entirety in the electronic edition of the *Astrophysical Journal*. A portion is shown here for guidance regarding its form and content.

[a]Photometric redshifts are enclosed in brackets.

The analysis of the number counts versus apparent magnitude suggests a significant evolution of the comoving number density of galaxies with an early-type morphology, scaling as $n\propto(1+z)^{-2.5}$. Similar results have been found using different approaches and datasets by other independent studies (e.g. Lin et al. 1999; Bell et al. 2004). Such an evolution should therefore be considered as a robust and important constraint to be reproduced by galaxy formation models.

For each galaxy in our final sample, we obtain an estimate of the zero point, slope and scatter of a range of colors from the available photometry of the ACS/GOODS database (B,V,i,z). These colors – given the redshift range of the sample ($z\lesssim1.5$) – map a rest frame wavelength range which straddles the age-sensitive 4000Å break. The zero point of each measurement is equivalent to the integrated color of the galaxy, and so it traces the bulk properties of the stellar populations. The slope of the radial gradient of the color accounts for age or metallicity variations and its evolution with redshift is a powerful discriminator among star formation histories (Tamura & Ohta 2000, Kodama & Arimoto 1997). The scatter can be used to track possible small episodes of star formation, as suggested by the line strength analysis of Trager et al. (2000)

The results are presented in figures 9, 10 and 11, with the remarkable finding of a clear cut segregation between the colors *and gradients* of the sample. This bimodality is strongly correlated with the type assigned from the photometric redshift estimate of Mobasher et al. (2004). Such correlation is robust with respect to the effects of the PSF, the galaxy luminosity or its size. The correlation of photometric type with color should not come as a surprise. However, the non-trivial finding is the correlation with color gradient: Galaxies with blue cores tend to be of later photometric types. A comparison with simple models of star formation in two bursts suggest that the blue subsample could represent a population of early-type galaxies which have experienced a recent episode of star formation in the recent ~1 Gyr. The fraction of these galaxies decreases as $z\to0$. Furthermore, figure 13 shows that these galaxies are the fainter ones, a result which is consistent with a lower star formation efficiency in low mass early-type galaxies. Figure 12 presents a strong constraint which should be imposed on models of galaxy formation. The color gradient is not found to undergo a strong redshift evolution, and is compatible with local early-type galaxies, assuming a radial gradient of metallicity, but not age. This trend is seen out to $z\sim1$. Furthermore, the color scatter does not evolve with redshift. This result along with the correlation between color and color gradient suggests an ordered inside-out formation process and the lack of mergers with star formation at $z\lesssim2$.

We would very much like to acknowledge the useful comments and suggestions from the referee, Dr. Eric Bell. T.L. acknowledges support by the Swiss National Science Foundation. This paper is based on observations made with the NASA ESA *Hubble Space Telescope*, obtained from the data archive at the Space Telescope Science Institute, which is operated by the Association of Universities for Research in Astronomy, Inc. under NASA contract NAS 5-26555. The HST ACS observations are associated with proposals 9425 and 9583 (the GOODS public imaging survey).

REFERENCES

Abraham, R. G., Valdes, F., Yee, H. K. C., van den Bergh, S., 1994, ApJ, 423, 75
Abraham, R. G., van den Bergh, S., Glazebrook, K., Ellis, R. S., Santiago, B. X., Surma, P. & Griffiths, R. E., 1996, ApJS, 107, 1
Baugh, C. M., Cole, S., Frenk, C. S. & Lacey, C. G., 1998, ApJ, 498, 504
Beers, T. C., Flynn, K. & Gebhardt, K., 1990, AJ, 100, 32
Bershady, M. A., Jangren, A., Conselice, C. J., 2000, AJ, 119, 2645
Bertin, E. & Arnouts, 1996, A&AS, 117, 393
Bell, E. F., et al. 2004, ApJ, 608, 752
Blakeslee, J. P., et al., 2003, ApJ, 596, L143
Bower, R. G., Lucey, J. R. & Ellis, R. S., 1992, MNRAS, 254, 189
Brinchmann, J. & Ellis, R. S., 2000, ApJ, 536, L77
Bruzual, G. & Charlot, S., 2003, MNRAS, 344, 1000
Cappellari, M. & Copin, Y., 2003, MNRAS, 342, 345

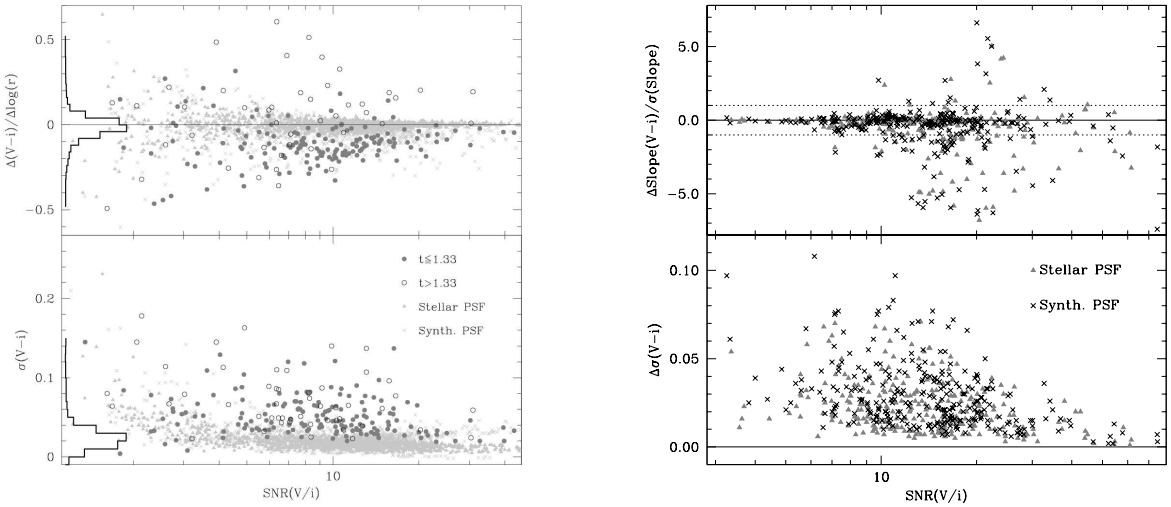

FIG. 15.— *Left:* Comparison of the $V-i$ radial slope and scatter as shown in figure 9 with respect to a synthetic sample of $> 1,500$ galaxies with zero color gradient and with the same noise behavior as the ACS/GOODS data: triangles (stellar PSF used in the analysis) and dots (Tiny-Tim PSF). *Right:* Recovery of the observed slopes in a sample of synthetic images with the same apparent magnitudes, sizes and noise characteristics as the original sample. Two different PSFs were used for the analysis, a stellar PSF as the one used in our analysis (triangles) and a synthetic one from Tiny-Tim (crosses).

Carollo, C. M., Danziger, I. J., & Buson, L., 1993, MNRAS, 265, 553
Carollo, C. M. & Danziger, I. J., 1994a, MNRAS, 270, 523
Carollo, C. M. & Danziger, I. J., 1994b, MNRAS, 270, 743
Cimatti, A., et al. 2002, A&A, 391, L1
Cimatti, A., et al. 2004, Nature, 430, 184
Conselice, C. J., Bershady, M. A., Jangren, A., 2000, ApJ, 529, 886
Conselice, C. J. 2003, ApJS, 147, 1
Conselice, C. J., Blackburne, J. A., Papovich, C., 2005, ApJ, 620, 564
de Lucia, G., et al. 2004, ApJ, 610, L77
Eggen, O. J., Lynden-Bell, D. & Sandage, A. R., 1962, ApJ, 136, 748
Eisenstein, D. J., et al. 2003, ApJ, 585, 694
Fasano, G., Cristiani, S., Arnouts, S. & Filippi, M., 1998, AJ, 115, 1400
Ferreras, I. & Silk, J. 2000a, MNRAS, 316, 786
Ferreras, I. & Silk, J. 2000b, ApJ, 541 L37
Ferreras, I. & Silk, J. 2003, MNRAS, 344, 455
Fontana, A., et al. 2004, A&A, 424, 23
Giavalisco, M. et al. 2004, ApJ, 600, L93
Gilli, R., et al. 2003, ApJ, 592, 721
Glazebrook, K., et al. 2004, Nature, 430, 181
Jørgensen, I., Franx, M. & Kjærgaard, P., 1995, MNRAS, 273, 1097
Kauffmann, G. & Charlot, S., 1998, MNRAS, 294, 705
Kodama, T. & Arimoto, N., 1997, A&A, 320, 41
Kodama, T., et al. 2004, MNRAS, 350, 1005
Kormendy, J. 1977, ApJ, 218, 333
Krist, J., 1993, ASP Conf. Ser. 52: Astronomical Data Analysis Software and Systems II, 2, 536
Kuntschner, H., 2000, MNRAS, 315, 184
La Barbera, F., Busarello, G., Merluzzi, P., Massarotti, M. & Capaccioli, M., 2003, ApJ, 595, 127
Le Fèvre, O., et al., 2004, A&A, 428, 1043
Lin, H., et al. 1999, ApJ, 518, 533
Lotz, J. M., Primack, J. & Madau, P. 2004, AJ, 128, 163
McIntosh, D. H., Zabludoff, A. I., Rix, H.-W. & Caldwell, N., 2005, ApJ, 619, 193
Marzke, R. O., da Costa, L. N., Pellegrini, P. S., Willmer, C. N. A. & Geller, M. J., 1998, ApJ, 503, 617
Menanteau, F., Abraham, R. G. & Ellis, R. S., 2001, MNRAS, 322, 1
Menanteau, F., et al. 2004b, ApJ, 612, 202
Mobasher, B., et al. 2004, ApJ, 600, L167
Peletier, R. F., Davies, R. L., Illingworth, G. D., Davis, L. E. & Cawson, M., 1990, AJ, 100, 1091
Press, W. H., Teukolsky, S. A., Vetterling, W. T. & Flannery, B. P. 1992, *Numerical Recipes in C*, Cambridge University Press
Schade, D., et al., 1999, ApJ, 525, 31
Somerville, R. S., Primack, J. R., 1999, MNRAS, 310, 1087
Somerville, R. S., Lee, K., Ferguson, H. C., Gardner, J. P., Moustakas, L. A. & Giavalisco, M. 2004, ApJ, 600, L171
Stanford, S. A., Eisenhardt, P, R. & Dickinson, M., 1998, ApJ, 492, 461
Tamura, N., Kobayashi, C., Arimoto, N., Kodama, T. & Ohta, K. 2000, AJ, 119, 2134
Tamura, N. & Ohta, K. 2000, AJ, 120, 533
Thomas, D., 1999, MNRAS, 306, 655
Thomas, D., Greggio, L. & Bender, R., 1999, MNRAS, 302, 537
Trager, S. C., Faber, S. M., Worthey, G. & González, J. J. 2000, AJ, 120, 165
Treu, T., Stiavelli, M., Casertano, S., Møller, P. & Bertin, G., 2002, ApJ, 564, L13
Trujillo, I. & Aguerri, J. A. L., 2004, MNRAS, 355, 82
van der Wel, A., Franx, M., van Dokkum, P. G. & Rix, H.-W. 2004, ApJ, 601, L5
van Dokkum, P. G. & Franx, M., Kelson, D. D. & Illingworth, G. D., 2001, ApJ, 553, L39
van Dokkum, P. G. & Franx, M. 2001, ApJ, 553, 90
Vanzella, E., et al. 2005, A&A, 434, 53
White, S. D. M. & Rees, M. J., 1978, MNRAS, 183, 341
Wuyts, S., van Dokkum, P. G., Kelson, D. D., Franx, M. & Illingworth, G. D., 2004, ApJ, 605, 677
Zheng, X. Z., Hammer, F., Flores, H., Assémat, F. & Pelat, D., 2004, A&A, 421, 847

APPENDIX

THE EFFECT OF THE SNR ON COLOR GRADIENTS AND SCATTER

We performed a set of simulations in order to assess the uncertainties related to the observed range of signal to noise ratios as well as the effect of the PSF and the pixel sampling. Four sets of galaxies each were generated, with a smooth surface brightness corresponding to a Sérsic profile with an index between $3-4$. Two tests were performed. In the first one we imposed a zero color gradient and no intrinsic scatter. We chose a random distribution of ellipticities and orientations, but the magnitudes and sizes corresponded to those from our sample. Each synthetic set thereby comprises 370 galaxies with an identical distribution of sizes and magnitudes as those of the real sample. In order to increase the statistical significance of the analysis we ran 4 such samples, for a total of $1,480$ galaxies. Noise was subsequently added to the image with the same distribution of SNR as a function of surface brightness as those obtained from the images and weight maps of the HST/ACS GOODS frames. Finally, we convolved the synthetic images with two choices of PSF, namely stellar – obtained from stars in the GOODS images with a high SNR — and synthetic – from TinyTim (Krist 1993). The resulting images followed the same pipeline analysis as the real galaxy sample. The results are shown in figure 15 (*left*), where the $V-i$ slope (*top*) and scatter (*bottom*) is shown as a function of SNR. The real data is overplotted – solid and hollow circles representing our sample of red and blue galaxies, respectively. The synthetic data are shown as triangles (stellar PSF) or crosses (synthetic PSF). One can see the increasing noise in the estimated slope and scatter towards lower SNR. The figure shows that the red/blue core separation as a function of photometric type is intrinsic to the galaxies.

We performed a second test on a synthetic sample with the same size, apparent magnitude *and color gradient* as our real sample. The procedure is equivalent as the one described above, and we show the results in figure 15 (*right*), where we plot in the top panel the difference between imposed and measured slope divided by the uncertainty. Notice that the quantity $\Delta\mathrm{Slope}(V-i)/\sigma(\mathrm{Slope})$ has a mean around zero and unit variance (-0.27 and 0.90, respectively, in the simulations). The bottom panel shows the measured scatter (the synthetic images use a smooth surface brightness profile but are affected by the noise). Notice the apparent larger scatter towards high SNR in the top panel. This is caused by an underestimate of the error bars in brighter galaxies. The actual difference between imposed and retrieved slopes *decreases* with increasing SNR. The number of outliers is consistent with the expected fraction. Inside the 1σ confidence level (dotted lines) we have $\sim 70\%$ of the complete sample.